Comparison between the Oxygen Reduction Reaction Activity of Pd$_5$Ce and Pt$_5$Ce: The Importance of Crystal Structure

Vladimir Tripkovic,*[†] Jian Zheng,[‡,||] Gian Andrea Rizzi,*[‡,||] Carla Marega,[‡] Christian Durante,[‡] Jan Rossmeisl,[†,§] and Gaetano Granozzi[‡]

[†]Center for Atomic-scale Materials Design, Department of Physics, Technical University of Denmark, DK-2800 Kongens Lyngby, Denmark

[‡]Department of Chemical Sciences, University of Padova, Via Marzolo, 1-35131 Padova, Italy

[§]Nano-Science Center, Department of Chemistry, University of Copenhagen, Universitetsparken 5, DK-2100 Copenhagen, Denmark

ABSTRACT: A set of electrochemical and X-ray spectroscopy measurements have been used conjointly with density functional theory (DFT) simulations to study the activity and stability of Pd$_5$Ce for the oxygen reduction reaction. A polycrystalline Pd$_5$Ce rod has been selected as a model catalyst to test if results on a several-fold activity increase of a series of Pt/rare-earth alloys hold also for Pd rare-earth alloys. Pd$_5$Ce crystallizes in two phases, a so-called low-temperature phase, L-Pd$_5$Ce, which has a cubic symmetry, and a high-temperature phase, H-Pd$_5$Ce, with a hexagonal symmetry. In both cases, a several-layers-thick Pd skin forms on the surface. Preliminary DFT results show that Pd overlayers under ≥2% compressive strain should be more active than Pt. In L-Pd$_5$Ce, the overlayer is under tensile strain, whereas in H-Pd$_5$Ce (a structure similar to Pt$_5$Ce), it is under compressive strain. We have confirmed that in our sample, L-Pd$_5$Ce is the dominant phase, both in the bulk and the outermost layers, while a H-Pd$_5$Ce-like phase is also present as a minor component far below the surface. Electrochemical ORR assessments show that the Pd overlayer in Pd$_5$Ce is less active than the polycrystalline Pd sample, in agreement with DFT results for the L-Pd$_5$Ce phase. Although we did not discover a new promising Pd-based catalyst, we have shown that the activity for oxygen reduction is strongly influenced by the alloy crystal structure. Furthermore, we have qualitatively demonstrated that transformation from H-Pd$_5$Ce to L-Pd$_5$Ce is more facile, requires less atom rearrangement, than transformation from Pt$_5$Ce to Pt$_3$Ce, which might explain the kinetic stability of Pt$_5$Ce at low temperatures.
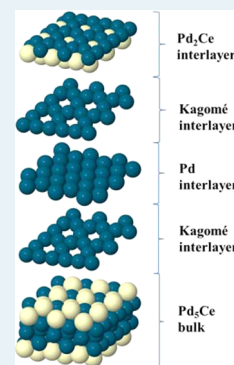
KEYWORDS: oxygen reduction reaction, fuel cell, cathode, Pd, Pt, alloys, rare-earth element

1. INTRODUCTION

A polymer electrolyte membrane fuel cell (PEMFC) is a device that can efficiently convert chemical into electrical energy with no or very low greenhouse gas emissions. At present, the main obstacle for a larger market share of PEMFCs is the high Pt loading at the cathode. Pt is a scarce and precious catalyst that adds substantial costs to PEMFCs. The catalyst loading at the cathode should be reduced by at least a factor of 4, while maintaining the current power output.[1] There are different strategies to accomplish this: mixing Pt with other noble and non-noble metal elements;[2−12] tailoring the size, shape, and interatomic distances of platinum and Pt-alloy nanoparticles;[1,13−19] or making nonsupported nanostructured catalysts.[20−24] Thus far, the best results are achieved for binary mixtures of Pt with Co or Ni.[3,21,25−27]

Pt alloys with rare-earth elements have shown great promise as cathode catalysts.[6,10,28] Binary transition metal alloys have been systematically screened for oxygen reduction reaction (ORR) activity in ref 11. The study was conducted assuming the same cubic L1$_2$ crystal structure for all the alloys. The outcome was that Pt$_3$Y and Pt$_3$Sc were more active and stable catalysts than Pt. As both Y and Sc are larger than Pt, the high activities at that point were assigned to a ligand effect coming

from subsurface Y and Sc. The ligand effect has to be fairly strong in order to overweight strain effect acting in the opposite direction. In a following study, it has been shown that the PtY alloy and its lanthanide analogues assume a different crystal structure that is not at all cubic but hexagonal, having the CaCu$_5$ structure. Formation of a several layers thick Pt overlayer at the surface of Pt rare-earth alloys was evidenced after leach-out of the rare-earth component.[29] Dissolution is restricted to a near-surface region due to high kinetic barriers for segregation from deeper layers, which in turn has been attributed to high alloy heat of formations. In a structure where rare-earth elements are buried several layers beneath the surface, the influence of a ligand effect is fully screened at the surface.[6] Therefore, the activity must be governed by strain which is conveyed from the bulk alloy onto the surface Pt overlayer. A compressively strained Pt overlayer is a result of lattice mismatch between the Pt overlayer and the bulk alloy.[6,10] The high activities of Pt rare-earth alloys are therefore associated with the distinct crystal structure in which the alloys

crystallize.[6,10] Because Pt rare-earth alloys have only recently been discovered, they are still at the early stages of development and testing. Particularly, more effort is needed to find a scalable chemical route to synthesize nanoparticles.[28] What prompted us to study Pd rare-earth alloys is the fact that Pd has a very similar electronic structure to Pt. As a matter of fact, Pd is the only metal, besides Pt, that makes intermetallic alloys with all rare-earth elements. We believed that alloying Pd with rare-earth metals could lead to a similar activity increase as in Pt rare-earth alloys.

In this contribution, we present results on the activity of a commercial Pd_5Ce polycrystalline sample using a combination of experimental analytical tools (X-ray diffraction, X-ray photoemission, and electrochemical measurements) and theoretical simulations. We argue the importance of bulk crystal structure for ORR activity and draw an analogy to Pt_5Ce and other Pt rare-earth alloys.

2. EXPERIMENTAL SECTION

The Pd_5Ce polycrystalline sample was purchased from Mateck GmbH and perchloric acid (70%) with ACS purity from Sigma-Aldrich. All solutions were prepared with Milli-Q water (18.2 MΩ·cm).

Before each electrochemical (EC) experiment, the Pd_5Ce sample was sputtered using a 0.5 keV beam of Ar^+ ions, until the surface was clean of adventitious contamination. The sputter-cleaned Pd_5Ce electrode was protected with a drop of Ar-saturated Milli-Q water and then transferred from UHV into a rotating disk electrode (RDE) assembly. A standard calomel electrode (SCE) inserted in a salt bridge was used in all measurements. Before each ORR experiment, the solution was bubbled with Ar for 1 h, and at least 100 CV scans were run until a stable CV curve was obtained. O_2 was then bubbled for 1 h until saturation. As a reference for the bulk Pd, we used a polycrystalline Pd (poly-Pd) electrode that was polished to 0.25 μm finish, cleaned with ethanol solution in an ultrasonic bath, rinsed with Milli-Q water, and lastly activated by cycling 100 times in 0.1 M $HClO_4$. A second series of experiments were carried out by transferring the sputter-cleaned Pd_5Ce sample from the UHV chamber into a custom-built EC flow microcell connected to an analysis chamber by a transfer mechanism. The obtained results were completely consistent with the ones obtained using the RDE assembly. The counter electrode was a Pt wire, and the reference electrode an Ag/AgCl electrode. All potentials reported in the text and figures are referred to the standard hydrogen electrode (SHE). All current densities were computed by normalizing to the geometrical surface area. All glassware was cleaned 24 h before the experiment with a $KMnO_4$ solution, rinsed with a 10% H_2O_2 solution, and lastly washed with Milli-Q water.

XRD patterns were recorded in the diffraction angular range 5−80° 2θ by a Philips X'Pert PRO diffractometer, working in the reflection or grazing angle geometry (incident angle α = 1°) and equipped with a graphite monochromator on the diffracted beam (Cu Kα radiation),

Angle-resolved X-ray photoemission spectroscopy (AR-XPS) measurements were performed on a custom-built UHV chamber (base pressure = 5×10^{-10} mbar) equipped with a nonmonochromatized double-anode X-ray source (Omicron DAR-400), a hemispherical electron analyzer (Omicron EA-125), a 5-channeltrons detection assembly, and a manipulator that allows to change the takeoff angles from 10° to 90°. The electron analyzer acceptance angle was ±4°, and the diameter of the analyzed area was 3 mm. Using the above-mentioned transfer system, XPS spectra (Al Kα) were recorded after the surface was sputter-cleaned, leached in acid solution ($HClO_4$ 0.1 M), and before and after ORR experiments. AR-XPS data were obtained (Al Kα) before and after EC measurements performed in a custom-made EC microcell connected to the UHV system by a leak-proof transfer mechanism. The binding energy scale was calibrated with respect to Pt $4f_{7/2}$, and all reported spectra intensities were obtained after a Shirley background subtraction. Assuming the well-known attenuation law for the Ce 3d signal, one can write the following equation:

$$I_{Ce3d} = \frac{I_{Ce3d(Pd_5Ce)}}{\cos \theta} \cdot \exp\left(-\frac{d}{\Lambda_{Ce}\cos \theta}\right) \qquad (1)$$

where I_{Ce3d} indicates the experimental intensity of Ce 3d, $I_{Ce3d(Pd_5Ce)}$ indicates the intensity of Ce 3d coming from the alloy without Pd-skin, modulated by the sampled area, Λ_{Ce} indicates the attenuation length in Pd-skin, and θ is the emission angle with respect to the surface normal. Finally, d is the thickness of Pd-skin. The Ce 3d intensities were fitted according to the above function, where d is the only fitting parameter, and $I_{Ce3d(Pd_5Ce)}$ is the experimental intensity of the sputter-cleaned surface of the alloy at 0°.

3. COMPUTATIONAL DETAILS

Total energies were calculated using Density Functional Theory (DFT) calculations employing a grid-based projector-augmented wave method (GPAW) code integrated with Atomic Simulation Environment (ASE).[30] Calculations were performed using the RPBE exchange−correlation functional[31] and the grid spacing of 0.15 Å. The RPBE relaxed lattice constant of Pd is 3.980 Å. Occupation of one-electron states is calculated at an electronic temperature of $k_BT = 0.1$ eV, and then extrapolated to $k_BT = 0$ K. Pd_5Ce is modeled as a strained Pd(111) slab separated by 12 Å vacuum in the surface normal direction. Pd(111) is the crystal face with the lowest surface energy and thus expected to dominate the surface. (It exhibits also the strongest signal in XRD − see Figure 7.) Strain was introduced by rescaling atom positions in the nonstrained Pd(111) surface corresponding to the amount of strain applied. The slab thickness was five layers. The bottom two layers were fixed, whereby the remaining atoms were allowed to relax in order to assume minimum energy positions. The Brillouin zone was sampled by a $4 \times 4 \times 1$ Monkhorst−Pack k-point grid.[32] The convergence was reached when the sum of absolute forces acting on the atoms was less than 0.05 eV Å^{-1}. Symmetry was applied to reduce the number of k-points in the Brillouin zone.

4. RESULTS AND DISCUSSION

We started out with DFT simulations in order to get a fast and robust estimate of catalyst performance using a simple model. The model demonstrated that compressively strained Pd overlayers should have high activities for ORR. As a model system, we selected the Pd_5Ce alloy because alloy components, Pd and Ce, crystallize in a hexagonal structure at the 5:1 atomic ratio. Hexagonal structure characterized by Pt atom vacancies (*Kagomé* layers) is considered to be the main reason for the high activities of Pt rare-earth alloys. Following the preliminary DFT analysis, a commercial Pd_5Ce sample was electrochemically tested in the RDE assembly. Afterward, the sample was transferred to the UHV chamber, where the surface was
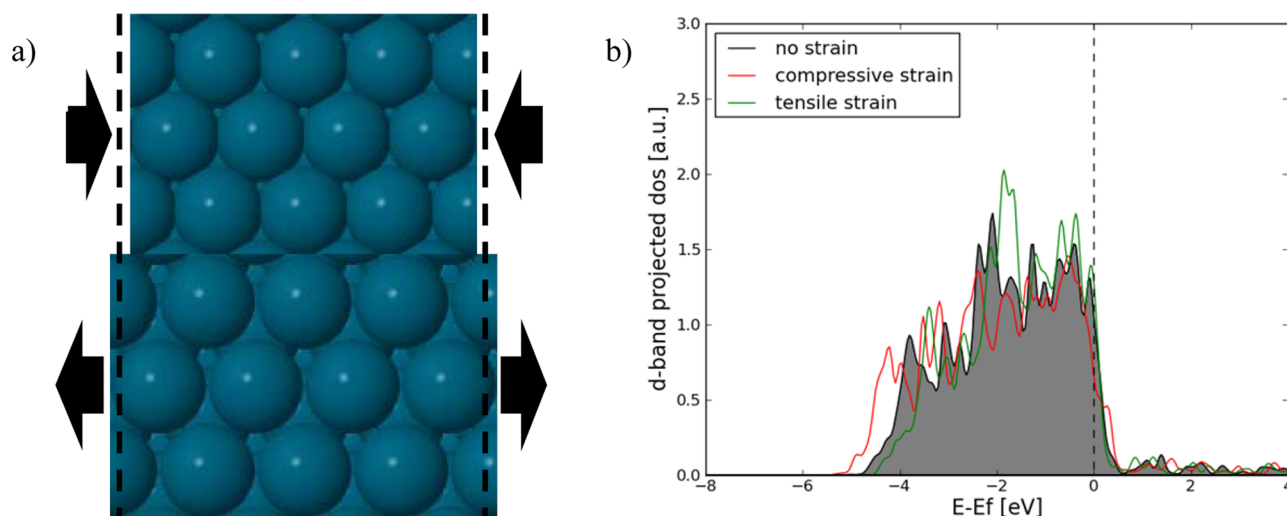
Figure 1. (a) Pd(111) slabs under different strain mimic Pd overlayers on-top of Pd rare-earth alloys. Dashed lines indicate the size of nonstrained Pd slab. (b) Projected density of states on the Pd d-band for pristine and slabs under 4% strain.
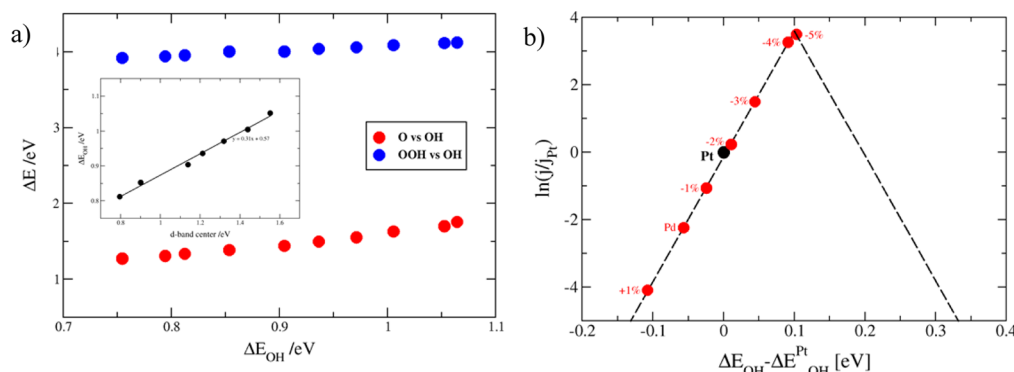

Figure 2. (a) Linear scaling relations between ORR intermediates and the OH binding energy and the d-band center in the inset. (b) Estimated activities of strained Pd(111) surfaces (red circles) as a function of the OH binding energy. Labels designate different strains, where "+" is expansive and "−" compressive strain.

characterized *in situ* using XPS (including AR-XPS) and *ex situ* using XRD. Finally, the structure found in the surface/bulk characterization experiments and ORR activities from electrochemical measurements were compared with activity estimates from atomic simulations.

Activity is governed by electronic structure of the catalyst surface.[33,34] There are two major electronic contributions that can impact the rate of the reaction: ligand and strain effect. The first effect is related to the influence of solute atoms on the electronic structure of the surface, whereas the other effect is related to strain imposed on the surface by an alloy underneath. Ligand effect is a short-ranged effect that is sizable only if solute atoms are directly beneath the surface or at most in the third surface layer.[35−37] Strain effect, on the other, hand is more long-ranged and can be conveyed up to 15 Å away from the point of its origin.[5,38] Several-layers-thick Pt-overlayers (four at least) were found to form on surfaces of Pt$_5$X (X − rare earth element), implying that ligand effect is not present at the surface.[10,29] The ORR activity is thus given by strain effect which is more withstanding. The fact that ligand effect is not present simplifies the model from having a full (alloy + Pd overlayer) system to having only Pd overlayers. It would be very hard to model the full system because lanthanide metals, which have unfilled f shells, are cumbersome to handle using DFT.

The amount of strain imposed on the Pd overlayer is inferred from the experimental "a" lattice parameter. Strain depends on the radius of lanthanide atoms, which decreases going from left to right in the lanthanide series. The effect of strain on the electronic structure of Pd is illustrated in Figure 1. Density of states (dos) for nonstrained Pd is shaded in gray, whereby dos of Pd slabs under 4% tensile and compressive strain are designated by green and red line, respectively. According to the d-band model the binding strength of an intermediate to a metal surface depends on the position of the metal d-band center.[33] The higher the d-band, the stronger the adsorbate binding. Shifts of d-bands can be easily discerned by looking at the onset of dos at −5 eV. For the compressively strained Pd slab (red line), the onset is shifted approximately 0.2 eV toward stronger binding values. A similar shift in the opposite direction is seen for the Pd slab under tensile strain (green line).

An activity estimation plot for ORR has been well-established in the past for transition metals and Pt alloys with transition metals.[7,26,39] The plot gives an estimate of the activity as a function of the binding energy (BE) of a chosen ORR intermediate. The plot assumes a volcano shape, suggesting an optimal BE. The volcano plot is a manifestation of Sabatier principle, which states that the best catalyst is the one that binds neither too weakly, so that a reaction can take place, nor too strongly, so that products can come off the surface.[40] The
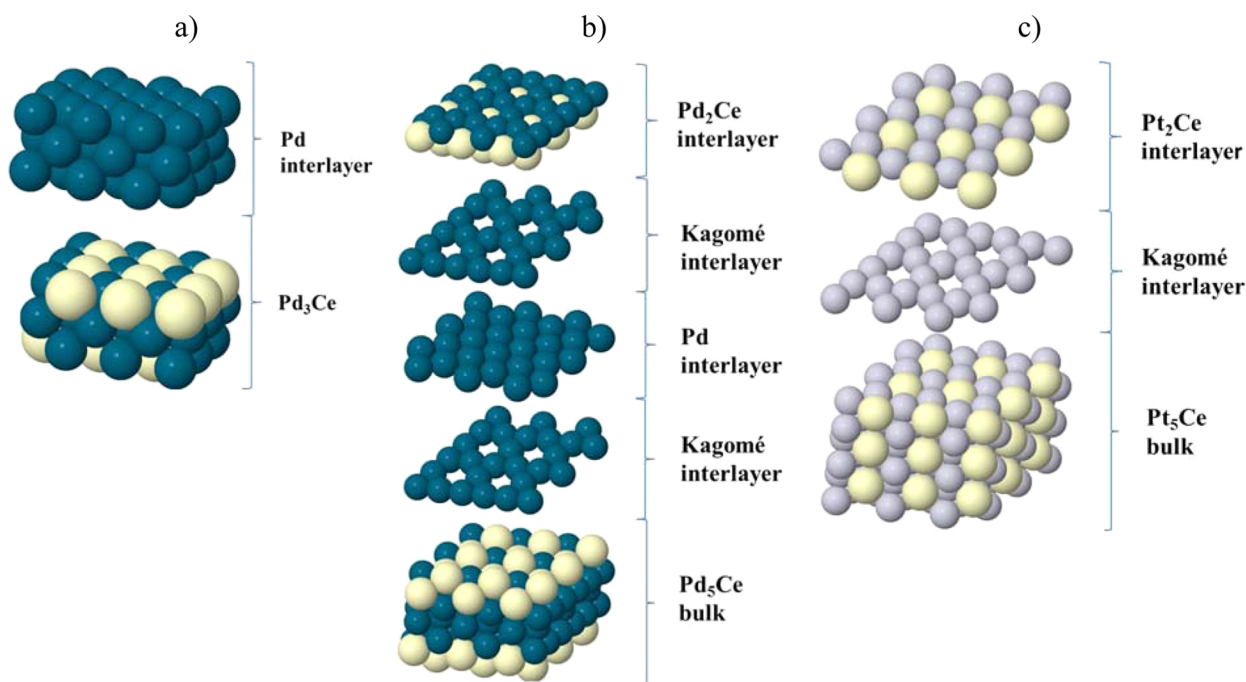
Figure 3. Illustrations showing (a) L-Pd$_5$Ce, (b) H-Pd$_5$Ce, and (c) Pt$_5$Ce bulk crystal structures. Dark blue, gray, and white spheres are Pd, Pt, and Ce atoms, respectively.

plot has been used for discovery of new catalysts in the past.[6,7,11,12,39] Here, we choose the OH binding energy as activity descriptor. It is also possible to use the d-band center or binding energy of any other ORR intermediate as activity descriptor, because in principle, all these quantities are linearly correlated and what we study here can be seen as a perturbation of pure Pd electronic structure.[33,41] Figure 2a shows linear correlations between different ORR intermediates, as well as a correlation between the OH binding energy and the d-band center (see the figure inset) as a function of strain. The OH binding energy has been calculated using water and hydrogen in the gas phase as references.[39] We have not explicitly considered solvent, because we assume that the influence of water on the OH binding energy is the same regardless of strain. Strain has been varied from −4% to +4%, where the "−" sign is for compressive and "+" sign for tensile strain. Imposing $a \geq 2\%$ compressive strain on the Pd surface should, according to the model in Figure 2b, render Pd(111) more active than Pt(111). Similarly; the Pd(111) surface under expansive strain should be less active than Pt(111) (black circle in Figure 2).

Choice of the Alloy. The optimal stoichiometric ratio between Pt and a rare earth element is 5:1.[42] At this atomic ratio, the alloys form a distinct hexagonal phase (CaCu$_5$ prototype structure) that has been assigned as the origin of high ORR activities.[6,10] According to Pd/rare-earth alloy phase diagrams, there are only four alloys (Pd$_5$Ce, Pd$_5$La, Pd$_5$Eu, and Pd$_5$Sm) that form hexagonal crystals at the 5:1 ratio.[43−46] All other Pd rare-earth alloys and alloys at ratios 5:1 or higher are derivatives of the L1$_2$ cubic structure. Because rare-earth atoms are larger than Pd, it is unlikely to expect that the alloys in the close-packed, L1$_2$ structure will show any activity enhancement compared to pure Pd. At lower atomic ratios than 5:1, the alloys corrode.[47]

Out of the four alloys, Pd$_5$Ce was selected for experimental testing. The case of Pt rare-earth alloys suggests that the choice of the alloy is not that important as long as the bulk structure is

hexagonal. However, Pd$_5$Ce crystallizes in two phases, a low-temperature phase, hereafter L-Pd$_5$Ce,[45] and a high-temperature phase, hereafter H-Pd$_5$Ce.[46] Bulk L-Pd$_5$Ce and H-Pd$_5$Ce structures are illustrated in Figure 3. L-Pd$_5$Ce has a cubic structure similar to L1$_2$. It consists of stacked Pd$_3$Ce layers, in which every third Pd$_3$Ce block has a Ce atom substituted by Pd, giving rise to the desired 5:1 stoichiometry. H-Pd$_5$Ce, on the other hand, has a hexagonal structure similar to Ni$_3$Ce, again with some Ce atoms substituted by Pd to give the right atomic ratio. In H-Pd$_5$Ce two adjacent Ce atoms are slightly shifted away from the plane in opposite directions as they cannot fit in the same layer with Pd atoms. The "layer" with Ce atoms is sandwiched by *Kagomé* layers that have atom vacancies below and above the positions of Ce atoms (see Figure 3b). Between the two *Kagomé* layers, there is a rotated, nondefective (no atoms missing) Pd layer. It is noteworthy that both *Kagomé* and nondefective layers have the same number of atoms, with one big difference (i.e., *Kagomé* layers are under compressive and nondefective layers under tensile strain). The sandwiched H-Pd$_5$Ce structure resembles the Pt$_5$Ce structure in the sense that it is also hexagonal and has *Kagomé* layers, but unlike Pt$_5$Ce, there is a layer under tensile strain. As mentioned earlier, bulk crystal structure determines strain imposed on the overlayer and thereby also ORR activity. Because Ce is larger than Pd, the Pd interlayer (after cleaving the crystal the interlayer becomes the overlayer) in L-Pd$_5$Ce is under tensile strain. It is not clear which strain dominates on the surface of H-Pd$_5$Ce, as there are layers under both compressive and tensile strain. To answer this question, we have mimicked dissolution of Ce atoms in H-Pd$_5$Ce by substituting them with Pd. After relaxation (energy minimization), the vacancies in *Kagomé* layers become filled with Pd atoms from the layers under tensile strain. This result suggests that a leached Pd$_5$Ce surface will form a compressively strained overlayer. The amount of strain was inferred by comparing experimental lattice parameters of L-Pd$_5$Ce, H-Pd$_5$Ce, and Pd and amounted to
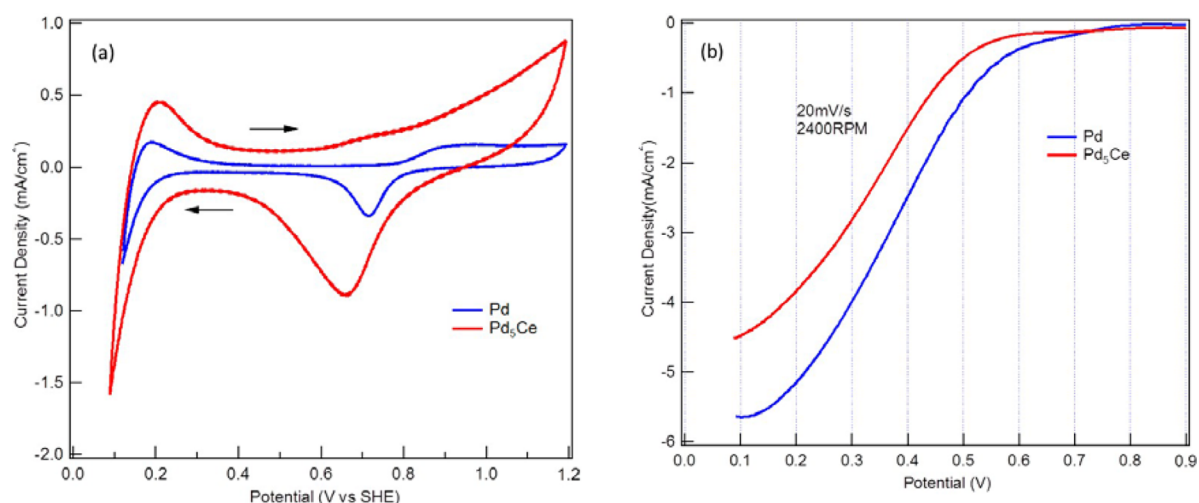
Figure 4. (a) Base voltammograms recorded in Ar-saturated 0.1 M HClO$_4$ solution at 50 mV/s for Pd and Pd$_5$Ce, (b) Polarization curves at 2400 rpm, 20 mV/s for the ORR on both electrodes in O$_2$-saturated 0.1 M HClO$_4$ solution.
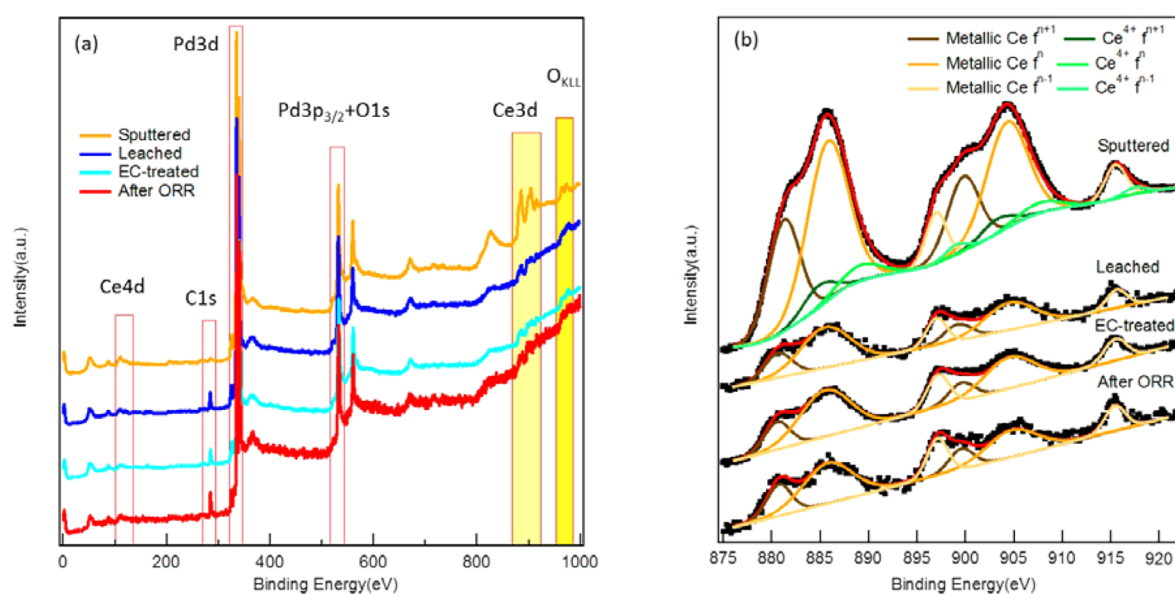
Figure 5. Photoemission of Pd$_5$Ce after different characterization and testing stages: "Sputtered", "Leached", "EC-treated", and "after ORR" notations stand for the Pd$_5$Ce sample after sputtering, acid leaching and electrochemical measurements in Ar and O$_2$ saturated solutions, respectively: (a) survey and (b) Ce 3d spectra with fitted components.

+3.3% in L-Pd$_5$Ce and −5.0% in H-Pd$_5$Ce. Given the opposite strain directions, the two Pd$_5$Ce phases should have very different activities for ORR. According to Figure 2b, the H-Pd$_5$Ce surface should be more active and L-Pd$_5$Ce less active than Pd.

Electrochemical Characterization. We set out to electrochemically test the sample. Prior to EC measurements, the Pd$_5$Ce sample was sputter-cleaned and preleached in Ar saturated 0.1 M HClO$_4$ solution. The ORR activity was measured after obtaining a stable base voltammogram and benchmarked to the poly-Pd sample (see Figure 4a). For more details about sample preparations, we refer to the Experimental Section.

Linear sweep voltammetry was used to evaluate the performance of the electrodes for ORR. Polarization curves at 2400 rpm for both electrodes are shown in Figure 4b. The onset potential for the reaction on Pd$_5$Ce is found at ∼0.65 V, a value about 0.15 V more negative than the one for Pd (∼0.80

V). From the results it is clear that Pd$_5$Ce is approximately 2 orders of magnitude less active for ORR than polycrystalline Pd. The low measured activity supports the notion that Pd overlayer on Pd$_5$Ce is under expansive strain. This is in contrast with results on Pt$_5$Ce,[29] Pt$_5$Gd,[10,29] Pt$_5$La,[6,29] and Pt$_5$Y[47] polycrystalline samples, in which highly active Pt overlayers under compressive strain have been suggested.

Surface/Bulk Characterization. The photoemission spectra were recorded at different stages of crystal preparation and testing: after sputter-cleaning, leaching in acid solution, during acquisition of CVs in Ar, and after ORR experiments. The survey spectra, displayed in Figure 5a, clearly indicate that the Ce 3d signals reduce dramatically after leaching. Furthermore, the spectra indicate that some adventitious carbon contamination is present at the surface after contact with acid solution and after EC measurements. The O$_{KLL}$ signal is always detected and can be assigned to oxygenated species from traces of water in the UHV chamber and from the electrolyte. Also, the XPS

Table 1. Photoemission Data of Various Ce Species in the Pd$_5$Ce Alloy after Different Treatments

	Ce				Ce^{4+}			
	f^{n+1}	f^{n}	f^{n-1}	total	f^{n+1}	f^{n}	f^{n-1}	total
BE (eV)	881.1	885.9	897.0		884.7	889.5	898.9	
sputtered	28%	51%	8%	87%	6%	5%	2%	13%
leached	21%	62%	17%	100%	-	-	-	-
EC-treated	19%	62%	19%	100%	-	-	-	-
after ORR	22%	56%	22%	100%	-	-	-	-

spectra before and after contact with acid solution are similar, which is an indication of that the surface composition is very stable during EC measurements.

The high-resolution photoemission spectra of Ce 3d (see Figure 5b) were acquired to obtain a more accurate surface composition after the various EC characterization steps. The Ce 3d spectra contain two components after sputtering (metallic Ce and Ce^{4+}) and only metallic Ce after contact with acid solution. The Ce 3d signal is composed of three doublets: f^{n+1}, f^{n}, and f^{n-1}, arising from various occupations of the Ce 4f orbitals.[29] The fitting results of Ce 3d are reported in Figure 5b and Table 1. The f^{n} component is the most intense one, whereas the f^{n+1} and f^{n-1}components are recognized as satellite peaks. According to the fitting results of the Ce 3d spectrum after sputtering, about 10% of the Ce amount in the alloy is present as CeO$_2$. After contact with acid solution, the Ce 3d spectrum corresponds only to metallic Ce, in the form of Pd$_5$Ce alloy.

The amounts of Pd and Ce were calculated after each of the four stages (see Table 2). After sputtering, the atomic contents

Table 2. Content of Pd and Ce after Each Treatment

|	Pd	Ce
sputtered	84%^{a}	16%
leached	93%	7%
EC-treated	94%	6%
after ORR	94%	6%

^{a}The theoretical ratio of Pd in the alloy is 83.3%.

of Ce and Pd are 16% and 84% respectively, a value consistent with the theoretical atomic ratio in Pd$_5$Ce. However, after leaching in acid solution, the amount of Ce decreases to 7%, about one-half of the amount after sputtering, implying a strong Ce depletion on the sample surface and formation of a Pd-skin structure. After performing the EC measurements the Ce amount reduces only slightly (from 7% to 6%), indicating that the surface composition is stable.

In Figure 6a, we report the Pd(3d)/Ce(3d) intensity ratio as a function of emission angles measured with respect to the surface normal. Clearly, after EC measurements the Ce 3d amount is strongly depleted in the near-surface region, which agrees well with what has previously been reported for Pt$_5$X alloys (i.e., the formation of a metal overlayer on the alloy).[6,29] We have obtained a Pd overlayer thickness of about 12.3 ± 1 Å (ca. 4 atomic layers of Pd) assuming formation of a sharp interface between the overlayer and the alloy (see Figure 6b).

In order to determine bulk crystal structure, the sample was further characterized by XRD.

XRD spectra of the Pd$_5$Ce sample in reflection and grazing angle geometries are presented in Figure 7. The dominant alloy phase is a cubic phase. The lattice parameter, "a", is estimated from the positions of the reflections to be 0.402 nm, which is comparable to the L1$_2$ phase of L-Pd$_5$Ce. Another phase was clearly detectable from the XRD pattern. Lower intensity reflections are attributable to an orthorhombic structure with lattice constants a = 0.520 nm, b = 0.909 nm, c = 1.769 Å, similar to the structure of H-Pd$_5$Ce. Thus, L- Pd$_5$Ce and H-Pd$_5$Ce are simultaneously present in the sample but with a clear prevalence of the cubic phase. Crystal plane indices of the two
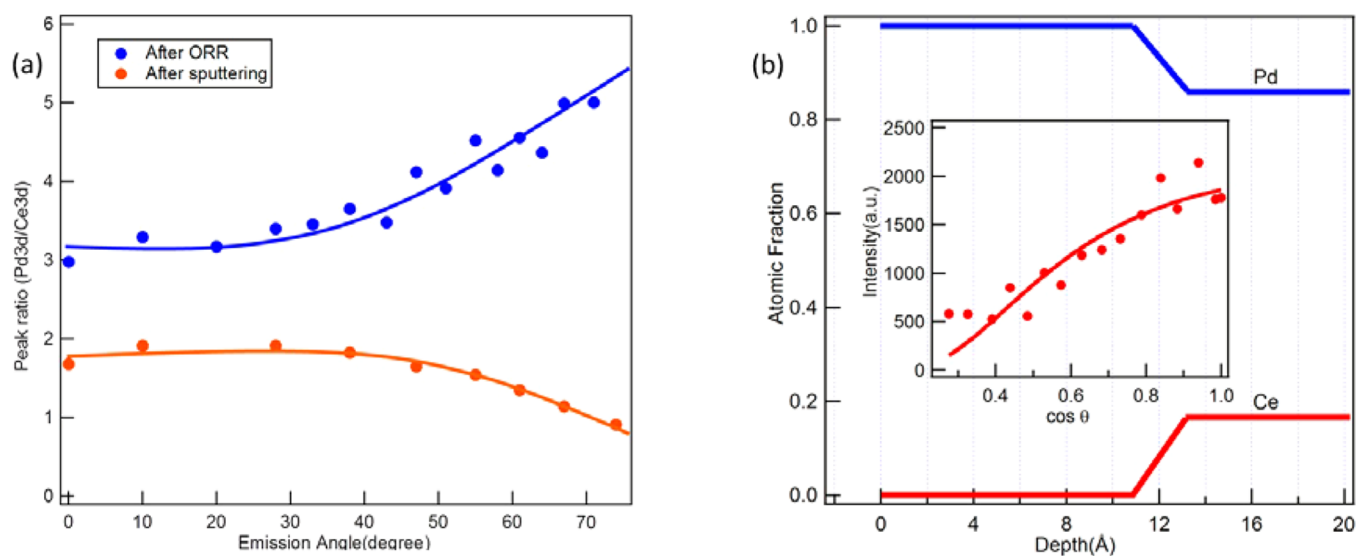
Figure 6. (a) AR-XPS of the Pd(3d)/Ce(3d) intensity y ratio and (b) schematic depth profiles after sputter cleaning and ORR measurements. The inset figure shows the fitting of experimental Ce 3d intensities.
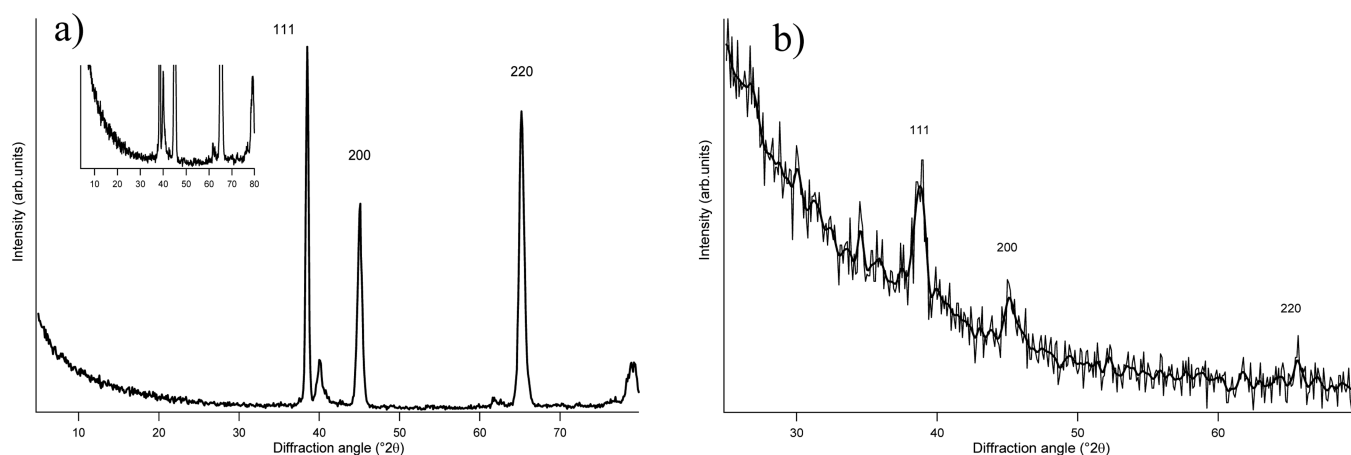
Figure 7. (a) XRD pattern (reflection geometry) of the Pd$_5$Ce sample. The inset is a magnification showing reflections of the orthorhombic phase. (b) XRD pattern (grazing angle geometry) for the commercial Pd$_5$Ce sample. Thicker line is the diffraction pattern after smoothing.

phases and incidence angles at which they appear are shown in Table 3.

Table 3. Diffraction 2θ Angles, Crystal Plane Indices, and Phases Present in the Pd$_5$Ce Sample

2θ	h k l	phase
38.5	1 1 1	cubic
40.0	1 3 4	orthorhombic
40.8	0 0 8	orthorhombic
42.6	0 4 3	orthorhombic
42.9	1 3 5	orthorhombic
45.1	2 0 0	cubic
61.6	3 3 0	orthorhombic
61.8	3 3 1	orthorhombic
62.6	3 3 2	orthorhombic
65.2	2 2 0	cubic
78.8	1 7 4	orthorhombic
79.2	3 5 4	orthorhombic

The grazing-angle XRD spectrum in Figure 7b shows that the only phase detectable at the surface (computed penetration depth was 125 nm) is the cubic one as only reflections corresponding to this phase are seen. Figure 7b shows the experimental spectrum superimposed on the same one after smoothing in order to better see the reflections. This is a necessary step because the amount of matter that scatters when using grazing angle geometry is low, and as a result, the registered spectrum is very poor.

Comparison between Theory and Experiments. The low measured ORR activity of the Pd$_5$Ce sample agrees with that predicted by DFT simulations for the L-Pd$_5$Ce phase. This is again in agreement with the XRD and XPS results showing that L-Pd$_5$Ce dominates the surface of the sample. Three other Pd rare-earth alloys that crystallize as high-temperature phases, H-Pd$_5$La, H-Pd$_5$Eu, and H-Pd$_5$Sm, will likely also spontaneously decay to less-active low-temperature phases. The question that arises is why then the same structure transition does not occur for Pt$_5$Ce?[29] The key for explaining different stabilities of Pt$_5$Ce and H-Pd$_5$Ce is in the slightly different crystal structures of the two alloys. In H-Pd$_5$Ce, Ce atoms lie next to each other in the same layer, whereas in Pt$_5$Ce, they are stacked on-top of each other, with Pt atom vacancies separating them (see Figure 3). Atom arrangement in H-Pd$_5$Ce strongly

resembles the one in the cubic L1$_2$ structure, suggesting that structure transformation from H-Pd$_5$Ce to L-Pd$_5$Ce is more facile than the one from Pt$_5$Ce to Pt$_3$Ce. It is hard to quantify kinetic barriers for structure reorganization because many atoms need to shift from their bulk positions. Performing energy minimization under applied strain can provide a hint on how much the atoms need to shuffle for Pt$_5$Ce and Pd$_5$Ce to convert into L1$_2$-like phases. As lanthanide metals are cumbersome to model in DFT, we have used Y instead of Ce. The analysis is for illustration purposes, and the type of rare-earth element will not affect the end result. To allow structure transformation, the unit cell parameters of H-Pd$_5$Y and Pt$_5$Y have been increased by 10%, because cubic close-packed structures have larger lattice constants than the hexagonal phases. Structures before and after energy minimizations are shown in Figure 8. As seen, H-Pd$_5$Y relaxes
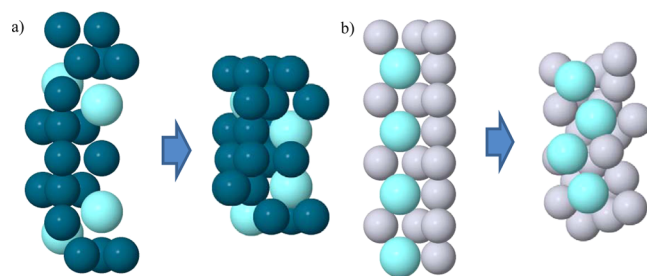
Figure 8. Initial and final structures of bulk (a) Pd$_5$Y and (b) Pt$_5$Y under 10% expansive strain, before and after energy minimization. Dark blue, gray, and cyan spheres are Pd, Pt, and Y atoms, respectively. It is explained in the text why Y is used instead of Ce.

to a close-packed structure that strongly resembles the L-Pd$_5$Y phase. Note that constraints imposed by the hexagonal unit cell prevent the full structure transition. After relaxation, the initial H-Pd$_5$Y becomes compressed along the height axis. As a consequence, the number of layers reduces from 8 to 6; Y atoms separate into two layers and vacant sites in *Kagomé* layers become filled by Pd atoms from the layers under tensile strains. Therefore, by compression along the height and some degree of atom exchange in the surface normal direction, H-Pd$_5$Ce can be readily transformed into a L-Pd$_5$Ce-like phase. In the case of Pt$_5$Y, the transformation cannot occur that easily because Y atoms are stacked along the same vertical axis. Moving Y atoms

one layer along the height is facile as there are vacancies below and above, but in order to create a L1$_2$-like phase, every second atomic plane has to drift one atomic position in order to maximize separation among Y atoms. In other words, a structure relaxation along both horizontal and vertical axis is needed to form the L1$_2$ phase. We believe the difference in bulk structures is the main reason why Pt$_5$Ce remains kinetically stable at low temperatures, whereas Pd$_5$Ce undergoes phase transformation.

In conclusion, the activity criterion for Pt/Pd rare-earth alloys is that the bulk structure contains *Kagomé* layers, because only if *Kagomé* layers are present, strain imposed on the surface is compressive, giving rise to high ORR activities (see Figure 2b). Both Pt$_5$Ce and Pd$_5$Ce alloys fulfill this requirement. Stability criterion, however, demands that the alloy assumes the CaCu$_5$ structure because only in this particular phase the alloy is kinetically stable at temperatures pertinent to low-temperature fuel cell operation. This criterion is fulfilled by Pt$_5$Ce and other Pt rare-earth alloys.

5. CONCLUSIONS

The study presented here is an example of a nicely carried out research project characterized by a close collaboration between theory, electrochemical testing, and surface characterization. The study was motivated by remarkable activity enhancements measured on polycrystalline Pt rare-earth samples. As a model system for Pd rare-earth alloys, we selected Pd$_5$Ce. DFT modeling pointed out that compressively strained Pd overlayers should be more active than Pt. However, the subsequent electrochemical analysis showed that the sample is even less active than Pd. Surface and bulk characterization experiments demonstrated the presence of two phases in the sample, H-Pd$_5$Ce and L-Pd$_5$Ce with a strong prevalence of the latter in bulk and even more at the surface. L-Pd$_5$Ce crystallizes in the cubic L1$_2$ structure, and the Pd overlayer that forms on-top of it is under tensile strain. Pd surface under tensile strain explains the observed activity decrease compared to nonstrained Pd. We argued the reason why a similar structure transformation does not occur in Pt rare-earth alloys, and we attributed that to the different arrangements of Ce atoms in the two hexagonal structures. Existence of *Kagomé* layers is a necessary but not a sufficient condition for attaining high ORR activities.

In summary, we have shown that the activity for oxygen reduction is strongly dependent on the bulk crystal structure and that the hexagonal CaCu$_5$ phase has a unique activity for the ORR.

■ AUTHOR INFORMATION

Corresponding Authors
*E-mail: tripce@gmail.com.
*E-mail: gianandrea.rizzi@unipd.it.
Author Contributions
‖Gian Andrea Rizzi and Jian Zheng equally contributed to the work.
Notes
The authors declare no competing financial interest.

■ ACKNOWLEDGMENTS

■ REFERENCES

(1) Gasteiger, H. A.; Kocha, S. S.; Sompalli, B.; Wagner, F. T. *Appl. Catal., B* **2005**, *56* (1−2), 9−35.

(2) Koh, S.; Strasser, P. *J. Am. Chem. Soc.* **2007**, *129* (42), 12624−12625.

(3) Stamenkovic, V. R.; Fowler, B.; Mun, B. S.; Wang, G. F.; Ross, P. N.; Lucas, C. A.; Markovic, N. M. *Science (Washington, DC, U. S.)* **2007**, *315* (5811), 493−497.

(4) Wang, C.; van der Vliet, D.; More, K. L.; Zaluzec, N. J.; Peng, S.; Sun, S. H.; Daimon, H.; Wang, G. F.; Greeley, J.; Pearson, J.; Paulikas, A. P.; Karapetrov, G.; Strmcnik, D.; Markovic, N. M.; Stamenkovic, V. R. *Nano Lett.* **2011**, *11* (3), 919−926.

(5) Strasser, P.; Koh, S.; Anniyev, T.; Greeley, J.; More, K.; Yu, C. F.; Liu, Z. C.; Kaya, S.; Nordlund, D.; Ogasawara, H.; Toney, M. F.; Nilsson, A. *Nat. Chem.* **2010**, *2* (6), 454−460.

(6) Stephens, I. E. L.; Bondarenko, A. S.; Grønbjerg, U.; Rossmeisl, J.; Chorkendorff, I. *Energy Environ. Sci.* **2012**, *5* (5), 6744−6762.

(7) Stephens, I. E. L.; Bondarenko, A. S.; Pérez-Alonso, F. J.; Calle-Vallejo, F.; Bech, L.; Johansson, T. P.; Jepsen, A. K.; Frydendal, R.; Knudsen, B. P.; Rossmeisl, J.; Chorkendorff, I. *J. Am. Chem. Soc.* **2011**, *133* (14), 5485−5491.

(8) Xue, L. Q.; Pang, X. Y.; Wang, G. C. *J. Phys. Chem. C* **2007**, *111* (5), 2223−2228.

(9) Sasaki, K.; Naohara, H.; Choi, Y.; Cai, Y.; Chen, W.-F.; Liu, P.; Adzic, R. R. *Nat. Commun.* **2012**, *3*, 1115.

(10) Escudero-Escribano, M.; Verdaguer-Casadevall, A.; Malacrida, P.; Grønbjerg, U.; Knudsen, B. P.; Jepsen, A. K.; Rossmeisl, J.; Stephens, I. E. L.; Chorkendorff, I. *J. Am. Chem. Soc.* **2012**, *134* (40), 16476−16479.

(11) Greeley, J.; Stephens, I. E. L.; Bondarenko, A. S.; Johansson, T. P.; Hansen, H. A.; Jaramillo, T. F.; Rossmeisl, J.; Chorkendorff, I.; Nørskov, J. K. *Nat. Chem.* **2009**, *1* (7), 552−556.

(12) Adzic, R. R.; Zhang, J.; Sasaki, K.; Vukmirovic, M. B.; Shao, M.; Wang, J. X.; Nilekar, A. U.; Mavrikakis, M.; Valerio, J. A.; Uribe, F. *Top. Catal.* **2007**, *46* (3−4), 249−262.

(13) Cui, C.; Gan, L.; Li, H.-H.; Yu, S.-H.; Heggen, M.; Strasser, P. *Nano Lett.* **2012**, *12* (11), 5885−5889.

(14) Nesselberger, M.; Roefzaad, M.; Faycal Hamou, R.; Ulrich Biedermann, P.; Schweinberger, F. F.; Kunz, S.; Schloegl, K.; Wiberg, G. K. H.; Ashton, S.; Heiz, U.; Mayrhofer, K. J. J.; Arenz, M. *Nat. Mater.* **2013**, *12* (10), 919−924.

(15) Shao, M. H.; Peles, A.; Shoemaker, K. *Nano Lett.* **2011**, *11* (9), 3714−3719.

(16) Tritsaris, G. A.; Greeley, J.; Rossmeisl, J.; Nørskov, J. K. *Catal. Lett.* **2011**, *141* (7), 909−913.

(17) Tripković, V.; Cerri, I.; Bligaard, T.; Rossmeisl, J. *Catal. Lett.* **2014**, *144* (3), 380−388.

(18) Wang, J. X.; Ma, C.; Choi, Y.; Su, D.; Zhu, Y.; Liu, P.; Si, R.; Vukmirovic, M. B.; Zhang, Y.; Adzic, R. R. *J. Am. Chem. Soc.* **2011**, *133* (34), 13551−13557.

(19) Wang, J. X.; Inada, H.; Wu, L. J.; Zhu, Y. M.; Choi, Y. M.; Liu, P.; Zhou, W. P.; Adzic, R. R. *J. Am. Chem. Soc.* **2009**, *131* (47), 17298−17302.

(20) Liu, W.; Rodriguez, P.; Borchardt, L.; Foelske, A.; Yuan, J.; Herrmann, A.-K.; Geiger, D.; Zheng, Z.; Kaskel, S.; Gaponik, N.; Kötz, R.; Schmidt, T. J.; Eychmüller, A. *Angew. Chem., Int. Ed.* **2013**, *52* (37), 9849−9852.

(21) Chen, C.; Kang, Y.; Huo, Z.; Zhu, Z.; Huang, W.; Xin, H. L.; Snyder, J. D.; Li, D.; Herron, J. A.; Mavrikakis, M.; Chi, M.; More, K. L.; Li, Y.; Markovic, N. M.; Somorjai, G. A.; Yang, P.; Stamenkovic, V. R. *Science* **2014**, *343* (6177), 1339−1343.

(22) Debe, M. K.; Schmoeckel, A. K.; Vernstrom, G. D.; Atanasoski, R. *J. Power Sources* **2006**, *161* (2), 1002−1011.

(23) Cui, C.-H.; Yu, S.-H. *Acc. Chem. Res.* **2013**, *46* (7), 1427−1437.

(24) Koenigsmann, C.; Sutter, E.; Chiesa, T. A.; Adzic, R. R.; Wong, S. S. *Nano Lett.* **2012**, *12* (4), 2013−2020.

(25) Mukerjee, S.; Srinivasan, S. *J. Electroanal. Chem.* **1993**, *357* (1−2), 201−224.

(26) Stamenkovic, V.; Mun, B. S.; Mayrhofer, K. J. J.; Ross, P. N.; Markovic, N. M.; Rossmeisl, J.; Greeley, J.; Nørskov, J. K. *Angew. Chem., Int. Ed.* **2006**, *45* (18), 2897−2901.

(27) Stamenkovic, V. R.; Mun, B. S.; Arenz, M.; Mayrhofer, K. J. J.; Lucas, C. A.; Wang, G. F.; Ross, P. N.; Markovic, N. M. *Nat. Mater.* **2007**, *6* (3), 241−247.

(28) Hernandez-Fernandez, P.; Masini, F.; McCarthy, D. N.; Strebel, C. E.; Friebel, D.; Deiana, D.; Malacrida, P.; Nierhoff, A.; Bodin, A.; Wise, A. M.; Nielsen, J. H.; Hansen, T. W.; Nilsson, A.; Stephens, I. E. L.; Chorkendorff, I. *Nat. Chem.* **2014**, *6* (8), 732−738.

(29) Malacrida, P.; Escudero-Escribano, M.; Verdaguer-Casadevall, A.; Stephens, I. E. L.; Chorkendorff, I. *J. Mater. Chem. A* **2014**, *2* (12), 4234−4243.

(30) Mortensen, J.; Hansen, L.; Jacobsen, K. *Phys. Rev. B: Condens. Matter Mater. Phys.* **2005**, *71* (3), 035109.

(31) Hammer, B.; Hansen, L.; Nørskov, J. *Phys. Rev. B: Condens. Matter Mater. Phys.* **1999**, *59* (11), 7413−7421.

(32) Monkhorst, H. J. *Phys. Rev. B* **1976**, *13*, 5188−5192.

(33) Hammer, B.; Nørskov, J. K. In *Advances in Catalysis, Vol 45*; Jentoft, F., Ed.; Elsevier: Amsterdam, 2000; Vol. *45*, pp 71−129.

(34) Nørskov, J. K.; Bligaard, T.; Rossmeisl, J.; Christensen, C. H. *Nat. Chem.* **2009**, *1* (1), 37−46.

(35) Schlapka, A.; Lischka, M.; Groß, A.; Käsberger, U.; Jakob, P. *Phys. Rev. Lett.* **2003**, *91*, 016101.

(36) Tripković, V.; Abild-Pedersen, F.; Studt, F.; Cerri, I.; Nagami, T.; Bligaard, T.; Rossmeisl, J. *ChemCatChem* **2012**, *4* (2), 228−235.

(37) Tripkovic, V.; Hansen, H. A.; Rossmeisl, J.; Vegge, T. *Phys. Chem. Chem. Phys.* **2015**, *17* (17), 11647−11657.

(38) Kitchin, J. R.; Nørskov, J. K.; Barteau, M. A.; Chen, J. G. *Phys. Rev. Lett.* **2004**, *93*, 156801.

(39) Nørskov, J. K.; Rossmeisl, J.; Logadottir, A.; Lindqvist, L.; Kitchin, J. R.; Bligaard, T.; Jonsson, H. *J. Phys. Chem. B* **2004**, *108* (46), 17886−17892.

(40) Sabatier, P. *Ber. Dtsch. Chem. Ges.* **1911**, *44*, 1984−2001.

(41) Abild-Pedersen, F.; Greeley, J.; Studt, F.; Rossmeisl, J.; Munter, T. R.; Moses, P. G.; Skulason, E.; Bligaard, T.; Nørskov, J. K. *Phys. Rev. Lett.* **2007**, *99*, 016105.

(42) Stephens, I. E. L.; Bondarenko, A. S.; Bech, L.; Chorkendorff, I. *ChemCatChem* **2012**, *4* (3), 341−349.

(43) Takao, K. *J. Mater. Sci.* **1990**, *25* (2B), 1255−1260.

(44) Sakamoto, Y.; Takao, K.; Takeda, S.; Takeda, T. *J. Less-Common Met.* **1989**, *152* (1), 127−138.

(45) Kuwano, N.; Higo, S.; Yamamoto, K.; Oki, K.; Eguchi, T. *Jpn. J. Appl. Phys.* **1985**, *24* (Part 2, No. 8), L663−L665.

(46) Itakura, M.; Hisatsune, Y.; Sato, H.; Kuwano, N.; Oki, K. *Jpn. J. Appl. Phys.* **1988**, *27* (Part 1, No. 4), 684−685.

(47) Stephens, I. E. L.; Bondarenko, A. S.; Bech, L.; Chorkendorff, I. *ChemCatChem* **2012**, *4* (3), 341−349.